

Acoustic Exponential Materials

Sichao Qu^{a,b,*}, Min Yang^{b,*}, Touryu Wu^b, Yunfei Xu^b, Nicholas X. Fang^{a,*}

^aDepartment of Mechanical Engineering, The University of Hong Kong, Pokfulam Road, Hong Kong, China

^bAcoustic Metamaterials Group Ltd., Data Technology Hub, TKO Industrial Estate, Hong Kong, China

Abstract

We present a framework model for predicting the wave scattering parameters of gradient materials with spatially exponential density and/or bulk modulus, which we term acoustic exponential materials. The core idea is to derive a modified transfer matrix by analytically generalizing the plane-wave eigenmodes from uniform to exponential materials. We demonstrate that the generality and accuracy of this model outperform two textbook theories, e.g., small reflection theory and transfer matrix method. Hence, our theory can enable rapid and accurate design of anti-reflection layer without large-scale optimization. As an experimental demonstration, we constructed an exponential anti-reflection meta-layer by stacking multiple acoustic dipoles in their nonresonant band, while taking into account thermoviscous dissipation. Remarkably, we observed an average reflection of 0.86% from 420 Hz to 10000 Hz. Our model deepens the fundamental understanding of gradient materials and provides a practical design scheme for designing broadband anti-reflection meta-layers.

Keywords: Exponential materials, Generalized eigenmodes, Impedance matching mechanism, Broadband anti-reflection effect, Acoustic metamaterials

Introduction

In wave physics, the proposal of gradient materials can be traced back to the late nineteenth century when Lord Rayleigh [1] and Fraunhofer [2] discovered that reflection from an interface between two uniform materials with distinct impedance can be suppressed by an intermediate gradient layer. Since then, various gradient materials have been designed and applied in both optic and acoustic systems [3, 4], with the applications such as optical fibers [5], light-emitting diodes [6], lens [7, 8], and absorbers [9, 10]. As an important class of gradient materials, exponential materials (EMs), are defined in acoustics as having density and/or bulk modulus that follow exponential spatial dependence. In fact, due to gravitational and related physical effects, EMs are ubiquitous on earth. For example, barometric formula predicts exponential air density of the atmosphere [11] and similar stratification phenomena exist in ground soil [12, 13] and marine sediment [14, 15]. From this perspective, predicting acoustic wave behaviors in EMs can be an essential part of our understanding of nature. Beyond the scientific curiosity, EMs are exceptionally useful due to its outstanding broadband anti-reflection property, which is highly desired

in diverse fields such as solar cell [16, 17], disordered media [18, 19], aberrating layer [20, 21], invisibility cloak [22], etc. Unlike the well-known quarter-wavelength impedance transformer [23], EMs do not rely on Fabry-Pérot resonance to realize impedance matching, thus overcoming the narrowband feature. Hence, it is of great interest to have a general theoretical model that can cover various gradient EMs. Small reflection theory (SRT) [23, 24], as a textbook theory, is a convenient tool to model gradient materials including EMs. However, as its name indicates, it is only valid when the reflection is small. In microwave engineering, SRT has been adopted to model multi-section Binomial and Chebyshev transformers [25, 26] with the assumption of constant refraction index, which is usually only applicable to TEM transmission lines [23, 24]. In many gradient materials, both refraction index and impedance (or density and bulk modulus) can be spatially non-uniform. Fortunately, transfer matrix method (TMM) [23, 27] can be an alternative textbook theory without the above assumptions, thus being general. However, TMM relies on the approximation by discretizing the continuous layer in a piecewise manner [28]. The inherent numerical error can be reduced only when the discretization mesh is fine enough, with the cost of surged complexity of calculation [29]. Therefore, from this point of view, the two common textbook theories are neither general nor efficiently

*Corresponding author(s).

Email addresses: qusichao@hku.hk (Sichao Qu), min@metacoust.com (Min Yang), nicxfang@hku.hk (Nicholas X. Fang)

accurate.

In this work, we addressed the previous limitations in the case of unidirectional EMs, whose acoustic properties (i.e., density and bulk modulus) can be simultaneously non-uniform. Starting from this general setup, we derived the analytical plane-wave eigenmodes of EMs, as a generalization from uniform materials. Based on this, we developed a modified transfer matrix method (MTMM) for predicting the scattering parameters of EMs. The proposed MTMM is applicable to all EMs and does not require discretization, i.e., mesh free, as it takes advantage of analytical eigenmodes. This enables accurate response capture while preserving model generality, allowing for the analytical design of anti-reflection layers without multi-parameter and large-scale optimization [30, 31]. As an experimental example, we designed a series of perforated plates in their nonresonant band towards exponential density. Then, each plate was treated as an acoustic dipole whose effective density can be manipulated by perforated porosity and unit size. We also included the loss induced by thermoviscous boundary layer to model the dispersion in the fabricated meta-layer. The prefix ‘meta’ here, borrowed from metamaterials [32, 33, 34], emphasizes that our material properties are regulated through structural design rather than chemical composition. Finally, impedance tube measurements confirmed the exponential effective property and the extremely broadband anti-reflection effect (average 0.86% and less than 10% from 420 Hz to 10000 Hz) in the fabricated sample, demonstrating the feasibility of using our theory as an effective design scheme.

Classification of exponential materials

Acoustic isotropic materials are characterized by the density ρ and bulk modulus κ . For ideal one-dimensional (1D) EMs, we define two material properties as the function of space:

$$\begin{cases} \rho(x) = \rho_0 \exp(\mu_1 x) \\ \kappa(x) = \kappa_0 \exp(-\mu_2 x) \end{cases}, \quad (1)$$

where ρ_0 and κ_0 are constant and real-valued reference material properties defined at $x = 0$. Based on this, we can write the corresponding characteristic impedance Z and refraction index n as

$$\begin{cases} Z(x) = Z_0 \exp\left[\frac{(\mu_1 - \mu_2)x}{2}\right] \\ n(x) = n_0 \exp\left[\frac{(\mu_1 + \mu_2)x}{2}\right] \end{cases}, \quad (2)$$

where $Z_0 = \sqrt{\rho_0 \kappa_0}$ and $n_0 = 1$. From Eq. (2), we can also obtain the related distribution of sound speed

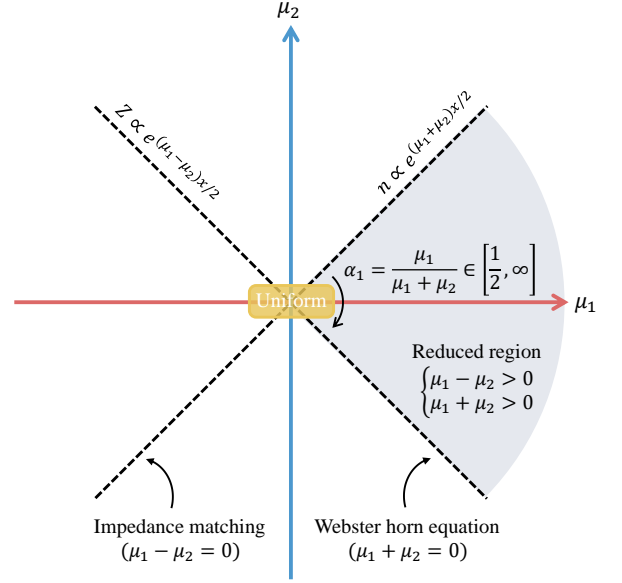


Figure 1: The classification of EMs by the parameter space of μ_1 and μ_2 , which are the measure of non-uniformity of exponential density and bulk modulus, respectively. In the center, $\mu_1 = \mu_2 = 0$, which represents the space for uniform materials. We define EMs in other spaces, i.e., the farther away from the origin the greater the non-uniformity.

$$c(x) = c_0 \exp\left[-\frac{(\mu_1 + \mu_2)x}{2}\right], \quad (3)$$

where $c_0 = \sqrt{\kappa_0/\rho_0}$.

Nevertheless, existing references tend to name their materials using either gradient impedance [35] or gradient index [36], while ignoring the other. Here, we show the necessity of considering both material properties to obtain a complete classification and to cover various EMs, as seen in the parameter space for classifying EMs in Fig. (1). Based on this, we can infer that an EM with pure exponential impedance requires that $\mu_1 - \mu_2 \neq 0$ and $\mu_1 + \mu_2 = 0$, while an EM with pure exponential index requires that $\mu_1 - \mu_2 = 0$ and $\mu_1 + \mu_2 \neq 0$. These two cases are represented by the two dashed lines in Fig. (1). Additionally, an EM with pure exponential density is located on the horizontal axis ($\mu_1 \neq 0, \mu_2 = 0$), while an EM with pure exponential bulk modulus is located on the vertical axis ($\mu_1 = 0, \mu_2 \neq 0$). If $\mu_1 = \mu_2 = 0$, EMs degenerate into uniform materials [at the center of Fig. (1)].

Wave equation with exponential properties

For 1D harmonic acoustic waves in the frequency domain, the momentum and constitutive equations [37] are

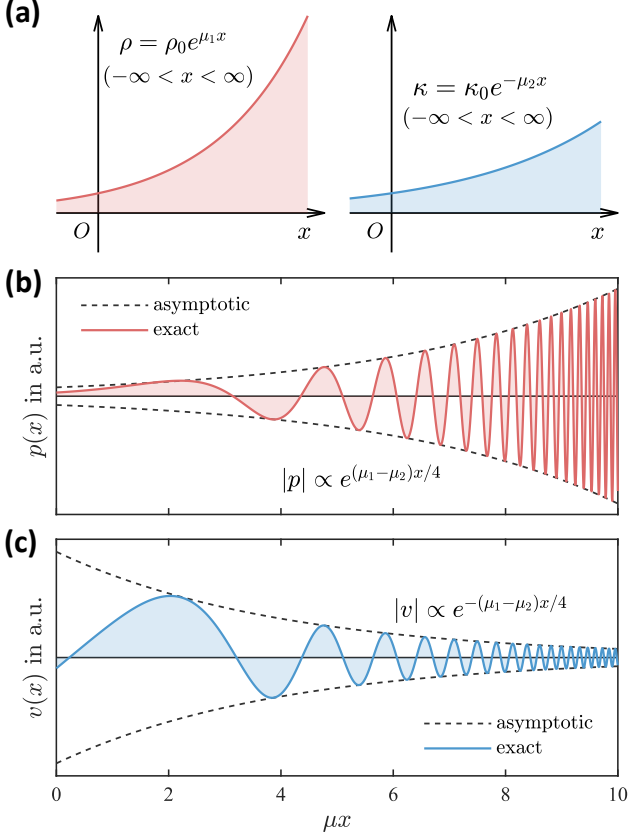


Figure 2: (a) The profiles of $\rho(x)$ and $\kappa(x)$ for an ideal and infinitely long EM in the reduce region in Figure (1). Here we take the values when $\mu_1 = -2\mu_2/3$ for example. (b-c) The calculated eigenmodes .i.e., pressure p and velocity v , in this EM at dimensionless frequency $\xi_0 = f/f_0 = 4/5$. The solid lines are real part of exact solution by Eq. (8), while the dashed lines are the absolute value of asymptotic solutions in Table. (1).

$$\begin{cases} -i\omega\rho(x)v + \partial_x p = 0 \\ -i\omega\kappa^{-1}(x)p + \partial_x v = 0 \end{cases}, \quad (4)$$

where $\rho(x)$ and $\kappa(x)$ follow exponential dependence in Eq. (1). By eliminating the particle velocity v , Eq. (4) can be reduced to wave equation with respect to p for non-uniform materials

$$\frac{\omega^2 p}{\kappa(x)} + \partial_x \left(\frac{1}{\rho(x)} \partial_x p \right) = 0. \quad (5)$$

Next, we examine the underlying symmetry by looking into the *duality* and *parity* of Eq. (4). First, by exchanging $p \leftrightarrow v$ and $\rho \leftrightarrow \kappa^{-1}$, we can witness the equation duality, which is the acoustic analogy of electric–magnetic duality (or Montonen–Olive duality) in Maxwell equation [27]. The underlying duality allows us to swap the wave equation solutions of v and p (and vice versa), by exchanging μ_1 and μ_2 . Second, we observe that the parity transformation ($x \leftrightarrow -x$) mathematically equals the sign reversal of non-uniformity parameters ($\mu_1 \leftrightarrow -\mu_1$ and $\mu_2 \leftrightarrow -\mu_2$). In Fig. (1), the two dashed lines divide the plane of

EMs into four problem region:

- A. $\mu_1 - \mu_2 > 0$ and $\mu_1 + \mu_2 > 0$;
- B. $\mu_1 - \mu_2 > 0$ and $\mu_1 + \mu_2 < 0$;
- C. $\mu_1 - \mu_2 < 0$ and $\mu_1 + \mu_2 > 0$;
- D. $\mu_1 - \mu_2 < 0$ and $\mu_1 + \mu_2 < 0$.

By leveraging the duality, we have the following problems equivalent: $A \Leftrightarrow C$ and $B \Leftrightarrow D$. Moreover, with parity symmetry, we have $A \Leftrightarrow D$ and $B \Leftrightarrow C$. Therefore, all possibilities of the solutions of Eq. (5) can be contained in the reduced region A [shadowed region in Fig. (1)]. This idea is similar to the concept of first Brillouin zone in solid state physics [38]. Hence, by taking advantage of symmetry, we can focus on reduced region where $\mu_1 - \mu_2 > 0$ and $\mu_1 + \mu_2 > 0$ throughout the followed contents, without the loss of generality.

Generalized plane-wave eigenmodes

To derive generalized plane-wave eigenmodes in an ideal, infinitely large EMs [see Fig. (2a)], we first define the following variable transformation

$$\begin{cases} \xi(x) = 2\omega / (c(x)\mu) \\ \alpha_1 = \mu_1 / \mu \\ \mu = \mu_1 + \mu_2 \end{cases}. \quad (6)$$

By assigning $x \rightarrow 0$, we define $\xi_0 = \xi|_{x=0} = f/f_0$, which can be regarded as the dimensionless frequency with the normalization factor $f_0 = c_0\mu/(4\pi)$. As shown in Fig. (1), α_1 can range from $\frac{1}{2}$ to ∞ in the reduced region. We use α_1 as a continuous index to quantify the type of EMs in the followed analysis. Then, the substitution of Eq. (1) into Eq. (5) yields a Bessel equation, whose general solution can be expressed as linear superposition of Bessel functions of first and second kinds [39]

$$p(x) = e^{\frac{\mu_1 x}{2}} [c_1 J_{\alpha_1}(\xi) + c_2 Y_{\alpha_1}(\xi)], \quad (7)$$

where we omit the harmonic dependence $\exp(-i\omega t)$. Eq. (7) can be interpreted as standing waves in EMs. Alternative, the corresponding traveling waves can be expressed by Hankel functions of the first and second kinds

$$p(x) = e^{\frac{\mu_1 x}{2}} [C_1 H_{\alpha_1}^{(1)}(\xi) + C_2 H_{\alpha_1}^{(2)}(\xi)]. \quad (8)$$

The interpretation of standing and traveling plane waves is justified by the extremum of power flow (see a rigorous proof in [Supplementary Materials](#), Section S1), which determines the conversion relation between (c_1, c_2) and (C_1, C_2) .

Properties	Uniform Materials $\rho = \rho_0, \kappa = \kappa_0$	Exponential materials (EMs) $\rho = \rho_0 e^{\mu_1 x}, \kappa = \kappa_0 e^{-\mu_2 x}$	
Solution type	Exact	Exact	Asymptotic ($\xi \gg 1$)
Pressure p (Standing wave)	$\begin{bmatrix} \sin(k_0 x) \\ \cos(k_0 x) \end{bmatrix}$	$e^{\frac{\mu_1 x}{2}} \begin{bmatrix} J_{\alpha_1}(\xi) \\ Y_{\alpha_1}(\xi) \end{bmatrix}$	$\left(\frac{2}{\pi \xi_0}\right)^{\frac{1}{2}} e^{\frac{(\mu_1 - \mu_2)x}{4}} \begin{bmatrix} \sin\left(\xi - \alpha_1 \frac{\pi}{2} - \frac{\pi}{4}\right) \\ \cos\left(\xi - \alpha_1 \frac{\pi}{2} - \frac{\pi}{4}\right) \end{bmatrix}$
Velocity v (Standing wave)	$\frac{1}{Z_0} \begin{bmatrix} \sin(k_0 x) \\ -\cos(k_0 x) \end{bmatrix}$	$\frac{-ie^{\frac{\mu_2 x}{2}}}{Z_0} \begin{bmatrix} J_{-\alpha_2}(\xi) \\ Y_{-\alpha_2}(\xi) \end{bmatrix}$	$\left(\frac{2}{\pi \xi_0}\right)^{\frac{1}{2}} \frac{-ie^{-\frac{(\mu_1 - \mu_2)x}{4}}}{Z_0} \begin{bmatrix} \sin\left(\xi + \alpha_2 \frac{\pi}{2} - \frac{\pi}{4}\right) \\ \cos\left(\xi + \alpha_2 \frac{\pi}{2} - \frac{\pi}{4}\right) \end{bmatrix}$
Pressure p (Traveling wave)	$\begin{bmatrix} e^{ik_0 x} \\ e^{-ik_0 x} \end{bmatrix}$	$e^{\frac{\mu_1 x}{2}} \begin{bmatrix} H_{\alpha_1}^{(1)}(\xi) \\ H_{\alpha_1}^{(2)}(\xi) \end{bmatrix}$	$\left(\frac{2}{\pi \xi_0}\right)^{\frac{1}{2}} e^{\frac{(\mu_1 - \mu_2)x}{4}} \begin{bmatrix} e^{i(\xi - \alpha_1 \frac{\pi}{2} - \frac{\pi}{4})} \\ e^{-i(\xi - \alpha_1 \frac{\pi}{2} - \frac{\pi}{4})} \end{bmatrix}$
Velocity v (Traveling wave)	$\frac{1}{Z_0} \begin{bmatrix} e^{ik_0 x} \\ -e^{-ik_0 x} \end{bmatrix}$	$\frac{-ie^{\frac{\mu_2 x}{2}}}{Z_0} \begin{bmatrix} H_{-\alpha_2}^{(1)}(\xi) \\ H_{-\alpha_2}^{(2)}(\xi) \end{bmatrix}$	$\left(\frac{2}{\pi \xi_0}\right)^{\frac{1}{2}} \frac{-ie^{-\frac{(\mu_1 - \mu_2)x}{4}}}{Z_0} \begin{bmatrix} e^{i(\xi + \alpha_2 \frac{\pi}{2} - \frac{\pi}{4})} \\ e^{-i(\xi + \alpha_2 \frac{\pi}{2} - \frac{\pi}{4})} \end{bmatrix}$

Table 1: Eigenmodes (p and v) of uniform and exponential materials ($e^{-i\omega t}$ omitted). The displayed analytical solutions for EMs are the generalized version of those in uniform materials. In uniform materials, the wavenumber is defined as $k_0 = \omega/c_0$. At the high frequency limit when $\xi \gg 1$, the asymptotic eigenmodes [39] in EMs share the similar forms with plane-wave solution in uniform materials. However, the amplitude of p (or v) is modulated by $e^{(\mu_1 - \mu_2)x/4}$ (or $e^{-(\mu_1 - \mu_2)x/4}$). The velocity fields are obtained by substituting p into the first line of Eq. (4) with the additionally defined $\alpha_2 = 1 - \alpha_1$.

In Table (1), we displayed the plane-wave eigenmodes with respect to p and v , of both uniform materials and EMs for comparison (the derivation is available in [Supplementary Materials](#), Section S2). In Figs. (2b) and (2c), we plot the real parts of forward p and v in an EM in reduced region of Fig. (1). The dashed lines represent the envelope of asymptotic forms [the last column of Table (1)]. Thus, we observe that asymptotic forms are of good approximation if $\xi \gg 1$. Our generalized plane-wave eigenmodes are universal for all EMs with arbitrary combination of μ_1 and μ_2 in Eq. (1). If $\mu_1 + \mu_2 = 0$ ($\alpha_1 \rightarrow \infty$), the problem is equivalent to that governed by Webster horn equation [40] for modeling the acoustic waves in the cross-section varying ducts.

Modified transfer matrix method

Model setup. As shown in Fig. (3a), the basic model setup involves considering two uniform materials with distinct material properties. The EM is embedded in between as an impedance transformer with thickness L , and the material properties are ensured to be continuously connected at the interfaces. In this way, the density and bulk modulus are defined as

$$\rho(x) = \begin{cases} \rho_0 & x \leq 0 \\ \rho_0 \exp(\mu_1 x) & 0 < x < L \\ \rho_0 \exp(\mu_1 L) & x \geq L \end{cases}, \quad (9)$$

$$\kappa(x) = \begin{cases} \kappa_0 & x \leq 0 \\ \kappa_0 \exp(-\mu_2 x) & 0 < x < L \\ \kappa_0 \exp(-\mu_2 L) & x \geq L \end{cases}. \quad (10)$$

As an additional constraint, we assume that the impedance contrast is a constant for all EMs with different testing α_1 , which

ensures that

$$\frac{Z_L}{Z_0} = \exp\left[\frac{(\mu_1 - \mu_2)L}{2}\right] = 7.4, \quad (11)$$

which we will use as a demonstration value for all followed numerical results.

Elements of modified transfer matrix. Since the analytical solutions obtained earlier in Table (1) are accurate and universal, we now establish a modified transfer matrix method (MTMM) by taking advantage of the generalized eigenmodes in EMs, to predict the scattering parameters. The uniform material on the left (or right) side is associated with Port 1 (or Port 2). The ABCD-matrix [23] of the 2-port system relates the fields at different ports in following way

$$\begin{pmatrix} \frac{p|_{x=0}}{\sqrt{Z_0}} \\ v|_{x=0} \sqrt{Z_0} \end{pmatrix} = \begin{pmatrix} A & B \\ C & D \end{pmatrix} \begin{pmatrix} \frac{p|_{x=L}}{\sqrt{Z_L}} \\ v|_{x=L} \sqrt{Z_L} \end{pmatrix}, \quad (12)$$

where A, B, C, D are dimensionless matrix elements that follows the convention of generalized scattering matrix formalism [23, 41] (to be specified). If we apply the incident excitation from left and right sides respectively, the linear superposition of p and v can be written as

$$\begin{cases} \begin{pmatrix} 1 + S_{11} \\ 1 - S_{11} \end{pmatrix} = \begin{pmatrix} A & B \\ C & D \end{pmatrix} \begin{pmatrix} S_{21} \\ S_{21} \end{pmatrix} \\ \begin{pmatrix} S_{12} \\ -S_{12} \end{pmatrix} = \begin{pmatrix} A & B \\ C & D \end{pmatrix} \begin{pmatrix} 1 + S_{22} \\ -(1 - S_{22}) \end{pmatrix} \end{cases}, \quad (13)$$

where S_{ij} are the scattering matrix elements whose absolute values squared represents the energy ratio from Port i to Port j . If $i = j$, $|S_{ii}|^2$ denotes the reflected energy ratio at Port i . By treating A, B, C, D as the known elements, we can attain the scattering matrix

Methods		ABCD-matrix	Reflection (S_{11})
Our theory	MTMM	$\frac{\pi\xi_0}{2} \begin{pmatrix} \sqrt{\frac{Z_L}{Z_0}} e^{\frac{\mu_2 L}{2}} \mathcal{F}(\alpha_1, -\alpha_2, \xi_0, \xi_L) & -i\sqrt{\frac{Z_0}{Z_L}} e^{\frac{\mu_1 L}{2}} \mathcal{F}(\alpha_1, \alpha_1, \xi_0, \xi_L) \\ -i\sqrt{\frac{Z_L}{Z_0}} e^{\frac{\mu_2 L}{2}} \mathcal{F}(-\alpha_2, -\alpha_2, \xi_0, \xi_L) & \sqrt{\frac{Z_0}{Z_L}} e^{\frac{\mu_1 L}{2}} \mathcal{F}(\alpha_1, -\alpha_2, \xi_L, \xi_0) \end{pmatrix}$ where $\mathcal{F}(v_1, v_2, x_1, x_2) = J_{v_1}(x_1) Y_{v_2}(x_2) - J_{v_2}(x_2) Y_{v_1}(x_1)$	Eq. (14)
Textbook	SRT	Not applicable	Eq. (17)
	TMM	$\begin{pmatrix} \frac{1}{\sqrt{Z_0}} & 0 \\ 0 & \sqrt{Z_0} \end{pmatrix} \prod_{n=1}^N \begin{pmatrix} \cos(k_n \frac{L}{N}) & -iZ_n \sin(k_n \frac{L}{N}) \\ -\frac{i}{Z_n} \sin(k_n \frac{L}{N}) & \cos(k_n \frac{L}{N}) \end{pmatrix} \begin{pmatrix} \sqrt{Z_L} & 0 \\ 0 & \frac{1}{\sqrt{Z_L}} \end{pmatrix}$	Eq. (14)

Table 2: The theories for modeling EMs. For modified transfer matrix method (MTMM), it is defined that $\xi_0 = \xi|_{x=0}$ and $\xi_L = \xi|_{x=L}$. For small reflection theory (SRT), there is no matrix element involved. For traditional transfer matrix method (TMM), the ABCD-matrix is obtained by multiplying N sub-matrices, with the mesh size of L/N . In the n th layer, the wavenumber $k_n = \omega \sqrt{\rho_n/\kappa_n}$ and the characteristic impedance $Z_n = \sqrt{\rho_n \kappa_n}$, where $\rho_n = \rho_0 \exp(\mu_1 n L/N)$ and $\kappa_n = \kappa_0 \exp(-\mu_2 n L/N)$.

$$\begin{cases} S_{11} = (A + B - C - D)/(A + B + C + D) \\ S_{12} = 2(AD - BC)/(A + B + C + D) \\ S_{21} = 2/(A + B + C + D) \\ S_{22} = (-A + B - C + D)/(A + B + C + D) \end{cases}. \quad (14)$$

The analytical forms of A, B, C, D elements of MTMM are given in Table (2), whose derivation has been placed in [Supplementary Materials](#), Section S3.

S-matrix analysis. Because our system is time-invariant, linear and with scalar material properties, the *reciprocity* holds [41], which ensures that $S_{12} = S_{21}$ [thus $AD - BC = 1$, according to Eq. (14)]. Therefore, the reciprocity can guarantee symmetrical transmission, i.e.,

$$|S_{12}|^2 = |S_{21}|^2. \quad (15)$$

Since the embedded EM is lossless, i.e., $\text{Im}(\rho) = 0$, $\text{Im}(\kappa) = 0$, the absorption inside the EM should be zero, thus $|S_{12}|^2 + |S_{11}|^2 = 1$ or $|S_{21}|^2 + |S_{22}|^2 = 1$. With the consideration of Eq. (15), we can conclude that

$$|S_{11}|^2 = |S_{22}|^2, \quad (16)$$

although $S_{11} \neq S_{22}$ due to the phase difference. It should be noted that Eq. (15) holds for all frequencies regardless of the types of the EM, while Eq. (16) is valid only when the EM is lossless (the case we focus on here). Symmetrical reflected energy allows us to focus on the case where the incident excitation is from only Port 1, without losing the generality.

Our model vs textbook theories. To compare the proposed MTMM with the two representative theories in textbooks, we treat the reflection spectra obtained from finite element method (FEM) model as the reference values. The commercial software, COMSOL Multiphysics, was utilized to implement FEM

calculation throughout the paper. To ensure the correctness of FEM, the adopted mesh size was sufficiently small compared to the wavelength λ . The related results are displayed by the solid lines in Figs. (3b) and (3c), for EMs with different α_1 . Remarkably, the corresponding data given by the first line of Eq. (14) [see MTMM results in Fig. (3c)] match the reference values for all α_1 at all frequencies, which shows the generality and accuracy of our theory.

For predicting reflection from impedance-varying materials, small reflection theory (SRT) is a widely-used lightweight method [23]. Its assumptions are that the reflection at each layer is a small quantity, and that wave speed c_0 (or n_0) is constant, i.e., $\alpha_1 = \infty$ in our definition. So, analytical solutions may be obtained for special impedance distribution $Z(x)$. For example, for the EMs we considered, the overall reflection coefficient has the following form [23, 24]

$$S_{11} = \frac{1}{2} \int_0^L e^{2ik_0 x} \frac{d}{dx} \ln \left(\frac{Z(x)}{Z_0} \right) dx = e^{ik_0 L} \frac{\ln(Z_L/Z_0)}{2L} \frac{\sin(k_0 L)}{k_0 L}, \quad (17)$$

where $k_0 = \omega/c_0$. As shown by the green dashed lines in Figs. (3b) and (3c), the data by SRT coincide with reference values only for $\alpha_1 \rightarrow \infty$ and when the reflection is lower than 0.05. This is consistent with the prescribed assumptions of SRT.

The second textbook method is traditional transfer matrix method (TMM), which requires piecewise discretization of the investigated materials. To yield S_{11} coefficient, TMM also follows the similar procedure of obtaining ABCD-matrix, using the same formula, i.e., Eq. (14). However, the overall ABCD-matrix is generated from the one-by-one multiplication of N sub-matrices. See the mathematical details of TMM in [Supplementary Materials](#), Section S3. As shown in Fig. (3b), when $N = 6$, reflection spectra by TMM is accurate at low frequencies ($\omega L/c_0 < 4$), while for high frequencies ($\omega L/c_0 > 4$),

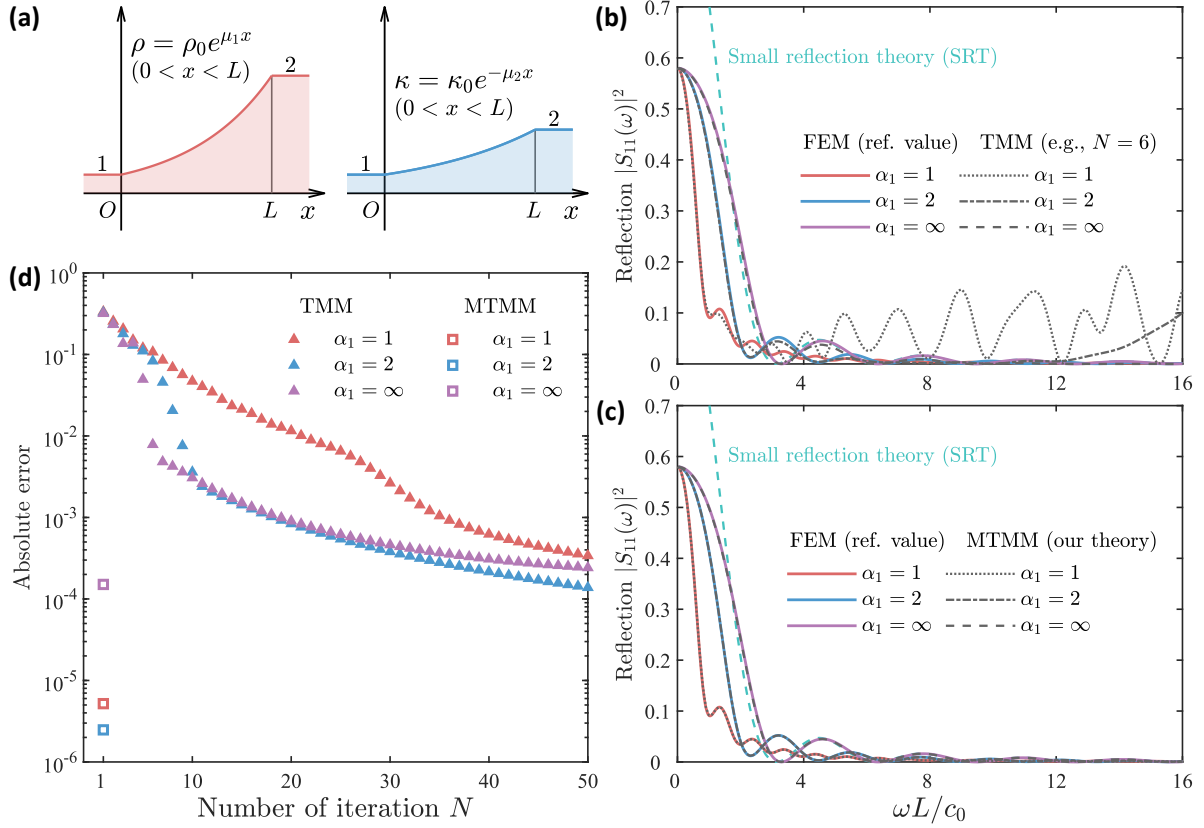


Figure 3: (a) The impedance transformer setup. The left and right sides are uniform materials with distinct material properties, which are connected with an EM. (b) The reflection $|S_{11}|^2$ predicted by traditional piece TMM ($N = 6$), compared with that by FEM as reference value. (c) The reflection $|S_{11}|^2$ predicted by MTMM and FEM. The green dashed lines in (b) and (c) are the same data given by SRT. (d) The absolute error of TMM and MTMM, plotted as function of iteration number N . The coefficient α_1 is adjusted for checking the generality and accuracy of different models.

TMM suffers from the discretization approximation. If $N = 50$, the error becomes low enough but the computation time is surged. Compared with SRT, TMM is general for all α_1 but the accuracy is not ensured if N is not sufficiently large.

From this perspective, SRT and TMM are neither general nor accurate. TMM can be general with cost of iteration times N . In Fig. (3d), we compare the absolute errors by TMM and MTMM in our case of EMs, respectively. Absolute errors denotes the frequency-averaged difference between the target theory and FEM. So, MTMM outperforms TMM because only one-step calculation is enough and the error of MTMM is smaller than that of TMM with even $N = 50$.

Broadband impedance matching mechanism

By equating left-side terms of Eq. (12) and the first line of Eq. (13), the reflection can be related with the specific impedance Z_s

$$S_{11} = \frac{Z_s - Z_0}{Z_s + Z_0}, \quad (18)$$

where $Z_s = (p/v)|_{x=0}$. The mechanism-level understanding impedance matching and anti-reflection performance of EMs in Fig. (3) requires analytical analysis on Z_s , which will be addressed next.

Low frequency behavior. If $\omega L / c_0 \rightarrow 0$, the ABCD-matrix of MTMM in Table. (2) becomes a diagonal matrix $\begin{pmatrix} \sqrt{Z_L/Z_0} & 0 \\ 0 & \sqrt{Z_0/Z_L} \end{pmatrix}$, which has been proved in the [Supplementary Materials](#), Section S3. According to Eq. (12), we conclude

$$\lim_{\omega \rightarrow 0} Z_s = Z_L, \quad (19)$$

thus yielding the reflection $S_{11} = (Z_L - Z_0)/(Z_L + Z_0) = 0.58$. So, we can interpret it as the ‘bypassing’ effect in EMs with our analytical model. From the perspective of impedance transfer, this means that the impedance at $x = L$ is transmitted unchanged to $x = 0$.

High frequency behavior. As shown in Fig. (3c), if $\omega L / c_0 \rightarrow \infty$, we observe a near-zero reflection in all EMs. Now we explain why. The ABCD-matrix of MTMM in Table. (2) at

the high frequency limit ($\omega \rightarrow \infty$) has the asymptotic values $A = D = 1$ and $B = C = 0$ (i.e. identity matrix). The related proof can also be found in the [Supplementary Materials](#), Section S3. By adopting these values into Eq. (12), we have

$$\lim_{\omega \rightarrow \infty} Z_s = Z_0 \frac{(p/v)|_{x=L}}{Z_L} = Z_0. \quad (20)$$

The last equal in Eq. (20) is because the continuity impedance ensured by Eq. (11), i.e., $(p/v)|_{x=L} = Z(L) = Z_0 e^{(\mu_1 - \mu_2)/2}$. This means that any end impedance will be transformed into the impedance that matches Port 1, i.e., analytical evidence of the excellent impedance-matching feature of EMs.

Intermediate frequency behavior. For the intermediate frequency range, we can see that impedance matching condition of Eq. (20) is still a good approximation. This also explains why gradually varying media always have excellent anti-reflection properties [4]. At high frequencies, the short wavelength makes it difficult to detect the non-uniformity of the material. As shown in Fig. (3c), it can be seen that the anti-reflection properties can be maintained over a wide frequency range, depending on how small of α_1 can be achieved. For instance, if we define f_1 as the threshold at which the reflection is below 0.1, then f_1 is lower and the anti-reflection effect is wider in bandwidth as α_1 approaches 1/2. In the following content, we will focus on the case where $\alpha_1 = 1$, which is an achievable target in airborne acoustics. Furthermore, we will also examine the case with lossy material properties and its impact on impedance matching.

Lossless and lossy EMs

We first consider a lossless EM with $\alpha_1 = 1$ with the following settings:

$$\begin{cases} \rho(x) = \rho_0 e^{\mu_1 x} \\ \kappa(x) = \kappa_0 \end{cases}, \quad (21)$$

$$\text{with } Z(L) = \frac{p}{v} \Big|_{x=L} = Z_0 e^{\mu_1 L/2}, \quad (22)$$

as shown in Fig. (4a). Here, we set the leaky impedance boundary as Eq. (22), following the same definition in Fig. (3a). The product $\mu_1 L$ should be determined by Eq. (11), i.e., $\mu_1 L = 4$.

We already know from Fig. (3d) about the excellent anti-reflection properties of such EM, and the same curve is displayed by blue data in Fig. (4e). Next, we consider the other lossy EM, with the settings:

$$\begin{cases} \rho(x) = \tilde{\rho}_0 e^{\mu_1 x} \\ \kappa(x) = \kappa_0 \end{cases}, \quad (23)$$

$$\text{with } Z(L) = \frac{p}{v} \Big|_{x=L} = \infty, \quad (24)$$

as shown in Fig. (4b). The proposed MTMM model is actually applicable to lossy EMs as well, but it requires complex $\tilde{\rho}_0$, whose dispersion should be determined by the concrete structures in real systems. For the subwavelength acoustic dipoles based on perforated plates that we will realize in the experiments, the dispersive material properties should adopt

$$\tilde{\rho}_0 = \rho_0 \left(1 + i \sqrt{\frac{\beta}{\omega}} \right), \quad (25)$$

where β is the dissipation factor. The derivation of Eq. (25) is available in [Supplementary Materials](#), Section S4. By replacing Eq. (21) by Eq. (23), we can actually predict the reflection of a lossy EM with the hard boundary Eq. (24) via MTMM.

Since the dissipation is inevitable in real sample, our motivation is to consider a lossy EM, whose β can be designed to make its reflection close to that of the corresponding lossless EM, with a leaky backing. It turns out that if $\beta = 630$ Hz, the approximation is observed to be valid when $\omega L/c_0 > 0.4$ [see Fig. (4e)]. It is displayed in Figs. (4c) and (4d) that the impedance spectra are also similar in the two cases, except the low frequency behaviors. The above results indicate that a finite lossy EM can mimic the reflection behavior of an ideal lossless EM with leaky backing boundary, laying the foundation for our experimental realization of anti-reflection meta-layer. It should be emphasized, however, that the suitable dissipation β of a lossy EM actually depends on the impedance contrast, which is already fixed by Eq. (11).

Experimental realization of anti-reflection meta-layer

Acoustic dipoles with tunable density. To realize the lossy EM in Fig. (4b) with excellent anti-reflection property, we seek real structures to realize these predetermined density properties. Therefore, the dipole candidate we found is the perforated plate [42], which is a type of acoustic dipole in airborne acoustic systems. The geometric parameters of a perforated plate include its thickness τ , hole diameter d , and the spacing a between holes. We also specify that the unit of the acoustic dipole is composed of air cavity with a length of ℓ . In addition, the porosity is the perforated area ratio $\phi = \pi d^2 / (2\sqrt{3}a^2)$ for hexagonal pore distribution. According to effective medium theory

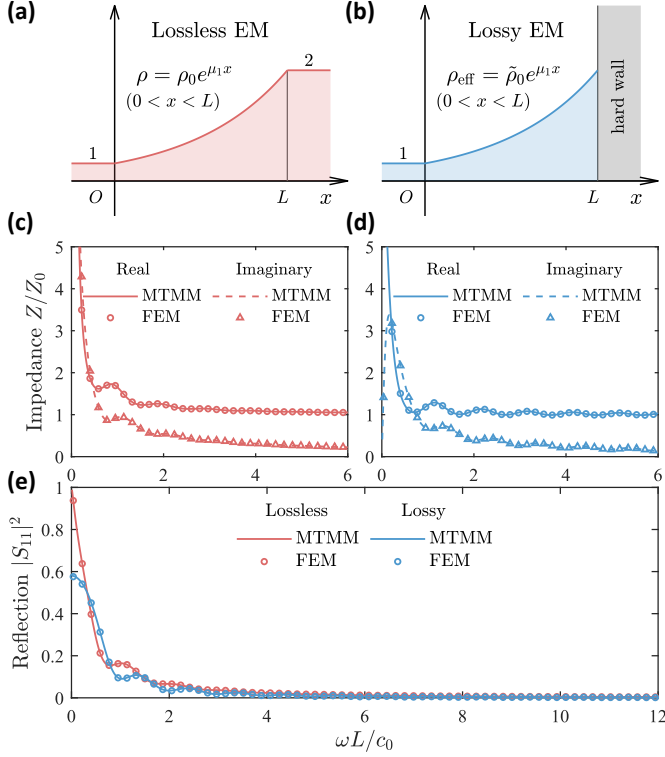


Figure 4: Lossless and lossy EMs with exponential density ($\alpha_1 = 1$). (a) The setup for a lossless EM backed by a leaky impedance boundary $Z(L) = Z_0 \exp\left[\frac{\mu_1 L}{2}\right]$. (b) The setup for a lossy EM with complex density $\tilde{\rho}_0 e^{\mu_1 x}$, backed by hard wall (i.e., $Z(L) \rightarrow \infty$). (c-d) The impedance spectra of lossless and lossy EMs in the setup of (a) and (b). (e) The reflection spectra of lossless and lossy EMs. The MTMM-predicted data agree well with those by FEM, showing the validity of our theory in lossy case.

(EMT) [43, 44, 45], in the non-resonant band, the effective bulk modulus of a perforated plate is the same as that of air¹, i.e., $\kappa_{\text{eff}} \cong \kappa_0$ due to the pure dipole nature. Here, the non-resonant band refers to the frequency range where $\ell \ll \lambda$ and the relevant effective properties are approximately non-dispersive. By contrast, the effective density is what we can regulate, which writes

$$\rho_{\text{eff}} = \frac{\rho_0}{\ell} \left[\ell - \tau + \frac{\tau + \delta\tau}{\phi} \left(1 + i \sqrt{\frac{\beta}{\omega}} \right) \right], \quad (26)$$

where the end correction $\delta\tau = 0.85dF(\phi)$ and the Fok function $F(\phi)$, depicting the interaction between the adjacent pores [46]. The first and second terms in Eq. (26) are contributed by air cavity and pore, respectively. The thermoviscous dissipation [45] in the pore was taken account by β . Here, we adopt $\beta = 8\nu/d^2$ and the kinematic viscosity $\nu = 1.59 \times 10^{-5} \text{ m}^2/\text{s}$. Derivation details of Eq. (26) can be found in [Supplementary Materials](#), Section S4. In our case, we obtain $d = 0.45 \text{ mm}$ by solving that

¹From now on, ρ_0 and κ_0 denote the density and bulk modulus of air, respectively.

$\beta(d) = 630 \text{ Hz}$. Here, the proper dissipation ensures the similarity between the reflection spectra in the lossy and lossless cases in Fig. (4). By adjusting ϕ and ℓ , we can manipulate the effective density over a wide range, thus acoustic dipole being tunable.

Design scheme. By utilizing the tunable acoustic dipoles, we can now construct an equivalent EM with gradient effective density. Our idea is to stack unit cells of different acoustic dipoles to create a meta-layer with a gradually varying effective property, in order to experimentally verify the anti-reflection effect shown in Fig. (4e). To inversely engineer geometric parameters of an array of perforated plates under the constraint of exponential density [see the fabricated sample photo in Fig. (5a)], we use n to label each perforated plate and related parameters (the total number $N = 39$). For example, the length of the n_{th} unit cell is ℓ_n , and the porosity of the n_{th} perforated plate is ϕ_n . Our strategy is to let the real part of Eq. (26) to follow exponential dependence

$$\exp(\mu_1 x_n) = \frac{1}{\ell_n} \left[\ell_n - \tau + \frac{\tau + \delta\tau(\phi_n)}{\phi_n} \right], \quad (27)$$

where x_n is the coordinate of n_{th} plate and we set $\tau = 0.7 \text{ mm}$. We set $x_1 = 0$, $x_2 = (\ell_1 + \ell_2)/2$, $x_n = (\ell_1 + \ell_n)/2 + \sum_{m=2}^{n-1} \ell_m$ ($n \geq 3$), and the total length $L = \ell_1/2 + \sum_{n=2}^N \ell_n$. To derive the design of ϕ_n , we can assign $\ell_n = \ell_1 e^{-\mu_1 x_n/3}$ and solve ℓ_1 by designating the total length $L = 0.2 \text{ m}$, which can determine $\mu_1 = 20 \text{ m}^{-1}$ according to Eq. (11). The necessity of introducing gradient ℓ_n lies in the fact that the wavelength will be suppressed if the sound speed becomes slower [see Figs. (2b) and (2c)]. In this way, the subwavelength condition ($\ell_n \ll \lambda$) can be maintained broadbandly. By numerically solving Eq. (27) for the roots, we can obtain a list of the required values of ϕ_n [see the outcome in Fig. (5b)]. As for the imaginary part of Eq. (26), if $\phi \ll 1$ (this is true for most plates), we can approximate Eq. (26) as the first line of Eq. (25). Hence, we can still use MTMM with the consideration of loss by Eq. (25) to model the meta-layer. In summary, in the design scheme, besides the plate thickness τ and total length L , all other geometric parameters are reverse-engineered rather than obtained through large-scale multi-parameter optimization. The detailed geometrical parameters are listed in [Supplementary Materials](#), Section S5.

Effective density characterization. We used 3D printing technology to fabricate individual perforated plates with pre-determined ϕ_n (The pore spacing was determined by $a_n = d[\pi/(2\sqrt{3}\phi_n)]^{1/2}$). We performed experimental measurements of the effective density for each individual plate before assem-

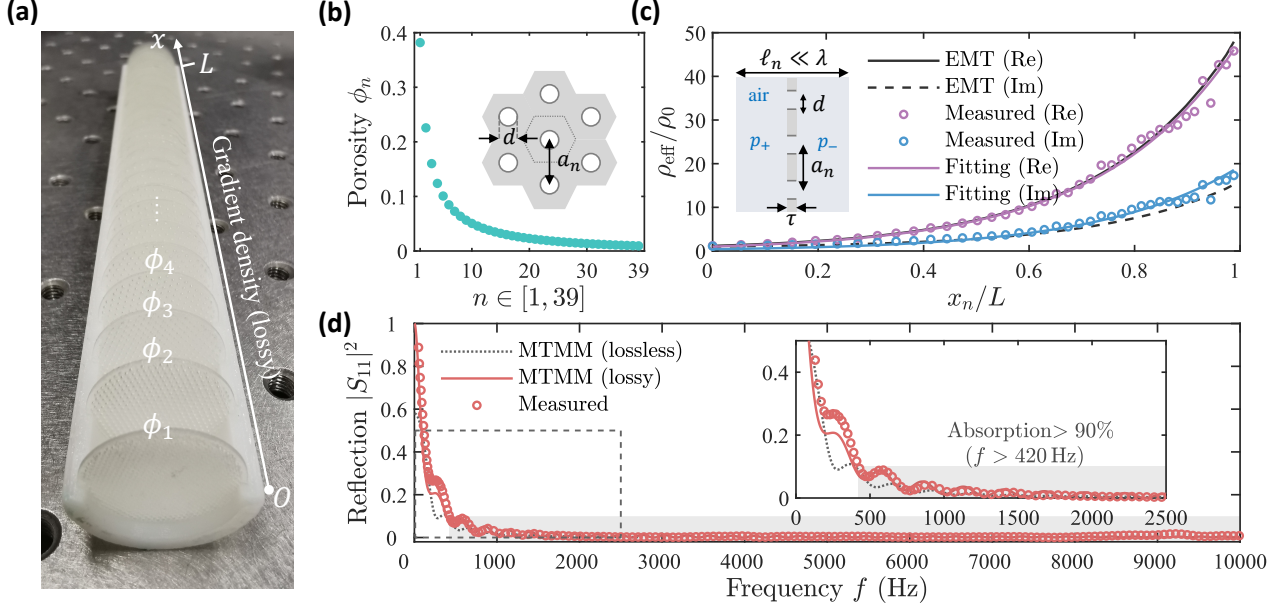


Figure 5: (a) The photo of the fabricated sample, with its cover removed for better illustration. The pore spacing is larger as the label n of ϕ_n increases. (b) The porosity distribution generated by the proposed design scheme. The inset depicts the front view of the perforated plate. (c) The measured effective density of individual unit cells at 1000 Hz, plotted as function of their location x_n . In addition, the obtained fitting function is $(1 + 0.04i) \exp(19.4 [\text{m}^{-1}]x)$. The inset is the side view of a unit cell. (d) The measured reflection of the overall assembled sample. The gray region from 420 Hz to 10000 Hz is determined by 10% reflection (or 90% absorption) as the threshold. The inset is an enlarged view of the low frequency spectrum.

bling individual perforated plates. The specific implementation was based on the four-microphone method via impedance tube to measure the reflection (S_{11}) and transmission (S_{21}) spectra (with phase information) of a single perforated plate at a measured frequency of 1000 Hz. Experimental details can be found in [Supplementary Materials](#), Section S6. According to Ref. [47], the measured effective density of the n_{th} plate is given by

$$\rho_{\text{eff}}(\omega) = i \frac{2Z_0}{\omega \ell_n} \frac{1 + (S_{11} - S_{21})}{1 - (S_{11} - S_{21})}. \quad (28)$$

It is shown in Fig. (5c) that the measured effective density (circles) indeed follows exponential spatial dependence. The black lines are the results predicted by EMT [see Eq. (26)]. We also fitted the measured real and imaginary parts of effective density by using exponential functions (purple and blue lines), which agree well with those by EMT. The above characterization experiment demonstrates the effectiveness of our design scheme.

Meta-layer preparation. To combine the individual fabricated perforated plates, we also printed two corresponding shell covers. The interior of the covers has designed grooves located at x_n for the installation of perforated plates. We used acoustic Plasticine to seal possible gaps and assembled all components to form the overall meta-layer. The bottom of the meta-layer is a hard wall [corresponding to the top of Fig. (5a)], and the incident port of the sound wave is the bottom of Fig. (5a). The

diameter of the internal cavity of the sample is 2 cm, which is aligned with the inner diameter of the circular impedance tube. The corresponding cut-off frequency of the impedance tube is 13950 Hz, which is enough to cover the range up to 10000 Hz, the upper limit of our measurement. To assemble the individual perforated plates, we printed two corresponding shell covers with designed grooves located at x_n . We used acoustic adhesive to seal possible gaps and assembled all components to form the overall meta-layer. The bottom of the meta-layer corresponds to the top of Fig. (5a), and the incident port of the sound wave is at the bottom of Fig. (5a). The diameter of the internal cavity of the sample is 2 cm, which is the same as the inner diameter of the circular impedance tube. The corresponding cut-off frequency of the impedance tube is 13950 Hz, which covers the range up to 10000 Hz, the upper limit of our measurement.

Reflection measurement. For the measurement of reflection, we used two-microphone method to evaluate the anti-reflection performance of the meta-layer. To cover such a broadband range, our experiments were carried out in two rounds (implementation details and equipment specifications available in [Supplementary Materials](#), Section S6). The experimental results show that the meta-layer possesses the low reflection of less than 10% from 420 Hz to 10000 Hz. Within this range, the averaged reflection $\int_{f_1}^{f_2} \frac{|S_{11}(f)|^2}{(f_2 - f_1)} df = 0.86\%$, where $f_1 = 420$ Hz and $f_2 = 10000$ Hz. The reflection tends to zero as the fre-

quency increases, which is consistent with our theoretical predictions [as shown in Fig. (5d) comparing the theoretical (red line) and experimental (red circles) data]. The theoretical results presented here used dimensional frequency as the horizontal axis, which are actually the same data from Fig. (4e). Because the end of the sample we designed is a hard wall, all incident energy except for the reflection will be absorbed. Compared with other competitive acoustic absorber/anti-reflection coatings, e.g., porous materials [48], absorbing metamaterials [49, 50, 51], our meta-layer has the largest relative bandwidth, i.e., $B_w = 2(f_2 - f_1)/(f_2 + f_1) = 1.84$, close to its upper limit 2.

Concluding remarks

Thus far, our results have shown an efficient and easily implementable way to achieve an EM-based anti-reflection meta-layer by manipulating the structure of multi-layer perforated plates. Other examples suitable for demonstrating more general acoustic EMs include temperature gradient pipes [52, 53], solid-fluid composites [54, 55, 56], and acoustic black holes [50, 57]. Furthermore, our acoustic theory can be easily extended to the case of electromagnetic waves by the following mapping

$$\begin{cases} \rho \rightarrow \epsilon \\ \kappa \rightarrow \mu^{-1} \end{cases}, \quad (29)$$

where ϵ , μ are the permittivity and permeability, respectively. The detailed derivations for the electromagnetic extension are available in the [Supplementary Materials](#), Section S7. Hence, the proposed MTMM-based design scheme, together with the excellent anti-reflection effect of EM, can have even broader impacts in microwave and optical metamaterials [3, 34, 58].

This article focuses on one-dimensional exponential material properties. Other types of functions, such as Pöschl–Teller function (sech^2 type) [59, 60] and power series [52, 61] were also examined. Additionally, Ref. [62] proposed a variational approach to yield optimal impedance profiles, and Ref. [63] systematically investigated the frequencies where waves can go around an obstacle. However, achieving broadband anti-reflection even for one-dimensional problems is not easy. Universal broadband impedance matching design were proposed in Refs. [36, 64]. Furthermore, Refs. [65, 66] demonstrated that if real and imaginary parts of the material parameters are associated by a spatial Kramer–Kronig relation, omnidirectional anti-reflection effects can be ensured with only passive components. For cases beyond one dimension, more general theories on reflectionless modes can include aspects in multi-mode

problems [67, 68], reciprocity constraints [69], and disordered media [18, 70, 71]. The development of transformation acoustics/optics [22, 72] can also be referenced for 2D and even 3D cases. However, achieving broadband effective properties in experiments is often challenging, and the required material properties can be anisotropic [22].

In conclusion, by taking advantage of the specific case of EMs, our work provides a foundational complement to previous studies from the analytical perspective. Under the condition of one-dimensional exponential material properties, we utilize generalized plane-wave eigenmodes as an effective theoretical analysis tool, to enhance our understanding of the impedance matching mechanism of traditional gradient materials. Simultaneously, we simplify the design procedure with the updated model, achieving unprecedented broadband anti-reflection performance. Looking ahead, EM can also be integrated as a key component into other anti-reflection devices. We expect that our acoustic-EM-based theoretical and experimental research paradigm can be extended to higher dimensions and other wave systems to generate profound impacts.

CRedit authorship contribution statement

Sichao Qu: Writing – original draft, Visualization, Methodology, Investigation, Formal analysis, Software, Conceptualization. **Min Yang:** Writing – review & editing, Formal analysis, Funding acquisition, Project administration, Conceptualization. **Touryu Wu:** Validation, Resources, Investigation, Data curation. **Yunfei Xu:** Validation, Resources, Investigation, Data curation. **Nicholas X. Fang:** Writing - review & editing, Formal analysis, Funding acquisition, Supervision, Project administration.

Declaration of competing interest

The authors declare that they have no known competing financial interests or personal relationships that could have appeared to influence the work reported in this paper.

Data availability

The data that support the findings of this study are available upon request from the corresponding authors.

Acknowledgements

S.Q. and M.Y. wish to thank Professor Ping Sheng for useful discussion on the design of multilayer perforated plates.

M. Y. acknowledges the Green Technology Fund (Grant number GTF202110282) from Environment and Ecology Bureau of Hong Kong Government for the funding support. N. X. F. acknowledges the startup support (Grant number GSP181), provided by Jockey Club Charities Trust STEM Lab of Scalable and Sustainable Photonic Manufacturing.

References

- [1] J. S. Rayleigh, Iv. on the intensity of light reflected from certain surfaces at nearly perpendicular incidence, *Proceedings of the Royal Society of London* 41 (1887) 275–294.
- [2] J. Fraunhofer, Joseph von Fraunhofer Gesammelte Schriften, Verlag der K. Akademie, Munich, Germany, 1888.
- [3] D. T. Moore, Gradient-index optics: a review, *Applied Optics* 19 (1980) 1035–1038.
- [4] Y. Jin, B. Djafari-Rouhani, D. Torrent, Gradient index phononic crystals and metamaterials, *Nanophotonics* 8 (2019) 685–701.
- [5] K. C. Kao, G. A. Hockham, Dielectric-fibre surface waveguides for optical frequencies, in: *Proceedings of the Institution of Electrical Engineers*, volume 113, IET, 1966, pp. 1151–1158.
- [6] A. Lenef, A. Piquette, J. Kelso, Thermodynamics of light extraction from luminescent materials, *ECS Journal of Solid State Science and Technology* 7 (2018) R3211.
- [7] S. Yang, J. H. Page, Z. Liu, M. L. Cowan, C. T. Chan, P. Sheng, Focusing of sound in a 3d phononic crystal, *Physical review letters* 93 (2004) 024301.
- [8] Q. Wu, J. M. Gibbons, W. Park, Graded negative index lens by photonic crystals, *Optics express* 16 (2008) 16941–16949.
- [9] F. Ding, Y. Cui, X. Ge, Y. Jin, S. He, Ultra-broadband microwave metamaterial absorber, *Applied physics letters* 100 (2012) 103506.
- [10] S. Ghaffari Mosanenzadeh, H. E. Naguib, C. B. Park, N. Atalla, Design and development of novel bio-based functionally graded foams for enhanced acoustic capabilities, *Journal of materials science* 50 (2015) 1248–1256.
- [11] M. N. Berberan-Santos, E. N. Bodunov, L. Pogliani, On the barometric formula, *American Journal of Physics* 65 (1997) 404–412.
- [12] R. Raspet, J. M. Sabatier, The surface impedance of grounds with exponential porosity profiles, *The Journal of the Acoustical Society of America* 99 (1996) 147–152.
- [13] K. Attenborough, Acoustical impedance models for outdoor ground surfaces, *Journal of Sound and Vibration* 99 (1985) 521–544.
- [14] I. Tolstoy, The theory of waves in stratified fluids including the effects of gravity and rotation, *Reviews of Modern Physics* 35 (1963) 207.
- [15] I. Tolstoy, Effect of density stratification on sound waves, *Journal of Geophysical Research* 70 (1965) 6009–6015.
- [16] D. J. Aiken, High performance anti-reflection coatings for broadband multi-junction solar cells, *Solar energy materials and solar cells* 64 (2000) 393–404.
- [17] Y. Tu, X. Tan, X. Yang, G. Qi, K. Yan, Z. Kang, Antireflection and radiative cooling difunctional coating design for silicon solar cells, *Optics Express* 31 (2023) 22296–22307.
- [18] M. Horodyski, M. Kühmayer, C. Ferise, S. Rotter, M. Davy, Anti-reflection structure for perfect transmission through complex media, *Nature* 607 (2022) 281–286.
- [19] M. A. Kats, R. Blanchard, S. Zhang, P. Genevet, C. Ko, S. Ramanathan, F. Capasso, Vanadium dioxide as a natural disordered metamaterial: perfect thermal emission and large broadband negative differential thermal emittance, *Physical Review X* 3 (2013) 041004.
- [20] C. Shen, J. Xu, N. X. Fang, Y. Jing, Anisotropic complementary acoustic metamaterial for canceling out aberrating layers, *Physical Review X* 4 (2014) 041033.
- [21] Y. Yang, H. Jia, W. Lu, Z. Sun, J. Yang, Impedance-matching acoustic bend composed of perforated plates and side pipes, *Journal of Applied Physics* 122 (2017).
- [22] H. Chen, C. T. Chan, Acoustic cloaking and transformation acoustics, *Journal of Physics D: Applied Physics* 43 (2010) 113001.
- [23] D. M. Pozar, *Microwave engineering*, John Wiley & sons, 2011.
- [24] K. Pendergraft, R. Pieper, An exact solution for a reflection coefficient in a medium having an exponential impedance profile, *The Journal of the Acoustical Society of America* 94 (1993) 580–582.
- [25] R. Collin, Theory and design of wide-band multisection quarter-wave transformers, *Proceedings of the IRE* 43 (1955) 179–185.
- [26] R. W. Klopfenstein, A transmission line taper of improved design, *Proceedings of the IRE* 44 (1956) 31–35.
- [27] J. D. Jackson, *Classical electrodynamics*, American Association of Physics Teachers, 1999.
- [28] D. Bethune, Optical harmonic generation and mixing in multilayer media: analysis using optical transfer matrix techniques, *JOSA B* 6 (1989) 910–916.
- [29] A. Luce, A. Mahdavi, F. Marquardt, H. Wankerl, Tmm-fast, a transfer matrix computation package for multilayer thin-film optimization: tutorial, *JOSA A* 39 (2022) 1007–1013.
- [30] S. W. Anzengruber, E. Klann, R. Ramlau, D. Tonova, Numerical methods for the design of gradient-index optical coatings, *Applied optics* 51 (2012) 8277–8295.
- [31] X. Guo, H. Zhou, S. Guo, X. Luan, W. Cui, Y. Ma, L. Shi, Design of broadband omnidirectional antireflection coatings using ant colony algorithm, *Optics express* 22 (2014) A1137–A1144.
- [32] J. Guo, Y. Fang, R. Qu, X. Zhang, Development and progress in acoustic phase-gradient metamaterials for wavefront modulation, *Materials Today* (2023).
- [33] M. Yang, P. Sheng, Acoustic metamaterial absorbers: The path to commercialization, *Applied Physics Letters* 122 (2023).
- [34] S. Qu, P. Sheng, Microwave and acoustic absorption metamaterials, *Physical Review Applied* 17 (2022) 047001.
- [35] P. C. Pedersen, O. Tretiak, P. He, Impedance-matching properties of an inhomogeneous matching layer with continuously changing acoustic impedance, *The Journal of the Acoustical Society of America* 72 (1982) 327–336.
- [36] K.-H. Kim, Q.-H. Park, Perfect anti-reflection from first principles, *Scientific reports* 3 (2013) 1–5.
- [37] A. N. Norris, Constant intensity acoustic propagation in the presence of non-uniform properties and impedance discontinuities: Hermitian and non-hermitian solutions, *The Journal of the Acoustical Society of America* 152 (2022) 2485–2492.
- [38] C. Kittel, P. McEuen, *Introduction to solid state physics*, John Wiley & Sons, 2018.
- [39] M. Stone, P. Goldbart, *Mathematics for physics: a guided tour for graduate students*, Cambridge University Press, 2009.
- [40] P. Martin, On webster’s horn equation and some generalizations, *The Journal of the Acoustical Society of America* 116 (2004) 1381–1388.
- [41] D. Jalas, A. Petrov, M. Eich, W. Freude, S. Fan, Z. Yu, R. Baets, M. Popović, A. Melloni, J. D. Joannopoulos, et al., What is—and what is not—an optical isolator, *Nature Photonics* 7 (2013) 579–582.
- [42] D.-Y. Maa, Potential of microperforated panel absorber, *the Journal of*

- the Acoustical Society of America 104 (1998) 2861–2866.
- [43] P. Cobo, F. Simón, Multiple-layer microperforated panels as sound absorbers in buildings: A review, *Buildings* 9 (2019) 53.
 - [44] M. Yang, G. Ma, Y. Wu, Z. Yang, P. Sheng, Homogenization scheme for acoustic metamaterials, *Physical Review B* 89 (2014) 064309.
 - [45] D. T. Blackstock, *Fundamentals of physical acoustics*, 2001.
 - [46] T. H. Melling, The acoustic impedance of perforates at medium and high sound pressure levels, *Journal of Sound and Vibration* 29 (1973) 1–65.
 - [47] M. Yang, C. Meng, C. Fu, Y. Li, Z. Yang, P. Sheng, Subwavelength total acoustic absorption with degenerate resonators, *Applied Physics Letters* 107 (2015).
 - [48] Y. Feng, D. Zong, Y. Hou, X. Yin, S. Zhang, L. Duan, Y. Si, Y. Jia, B. Ding, Gradient structured micro/nanofibrous sponges with superior compressibility and stretchability for broadband sound absorption, *Journal of Colloid and Interface Science* 593 (2021) 59–66.
 - [49] M. Yang, S. Chen, C. Fu, P. Sheng, Optimal sound-absorbing structures, *Materials Horizons* 4 (2017) 673–680.
 - [50] X. Zhang, L. Cheng, Broadband and low frequency sound absorption by sonic black holes with micro-perforated boundaries, *Journal of Sound and Vibration* 512 (2021) 116401.
 - [51] Z. Zhou, S. Huang, D. Li, J. Zhu, Y. Li, Broadband impedance modulation via non-local acoustic metamaterials, *National Science Review* 9 (2022) nwab171.
 - [52] Z. Musielak, D. Musielak, H. Mobashi, Method to determine cutoff frequencies for acoustic waves propagating in nonisothermal media, *Physical Review E* 73 (2006) 036612.
 - [53] R. Sujith, G. Waldherr, B. Zinn, An exact solution for one-dimensional acoustic fields in ducts with an axial temperature gradient, *Journal of Sound and Vibration* 184 (1995) 389–402.
 - [54] F. Cervera, L. Sanchis, J. Sánchez-Pérez, R. Martínez-Sala, C. Rubio, F. Meseguer, C. López, D. Caballero, J. Sánchez-Dehesa, Refractive acoustic devices for airborne sound, *Physical review letters* 88 (2001) 023902.
 - [55] A. A. Krokhin, J. Arriaga, L. Gumen, Speed of sound in periodic elastic composites, *Physical review letters* 91 (2003) 264302.
 - [56] J. Mei, Z. Liu, W. Wen, P. Sheng, Effective mass density of fluid-solid composites, *Physical review letters* 96 (2006) 024301.
 - [57] A. Pelat, F. Gautier, S. C. Conlon, F. Semperlotti, The acoustic black hole: A review of theory and applications, *Journal of Sound and Vibration* 476 (2020) 115316.
 - [58] G. V. Eleftheriades, Em transmission-line metamaterials, *Materials today* 12 (2009) 30–41.
 - [59] J. Lekner, Reflectionless eigenstates of the sech² potential, *American Journal of Physics* 75 (2007) 1151–1157.
 - [60] L. Thekketkara, V. G. Achanta, S. D. Gupta, Optical reflectionless potentials for broadband, omnidirectional antireflection, *Optics Express* 22 (2014) 17382–17386.
 - [61] M. B. Soley, C. M. Bender, A. D. Stone, Experimentally realizable p t phase transitions in reflectionless quantum scattering, *Physical Review Letters* 130 (2023) 250404.
 - [62] R. P. Erickson, Variational theory of the tapered impedance transformer, *Journal of Applied Physics* 123 (2018).
 - [63] A.-S. B.-B. Dhia, L. Chesnel, V. Pagneux, Trapped modes and reflectionless modes as eigenfunctions of the same spectral problem, *Proceedings of the Royal Society A: Mathematical, Physical and Engineering Sciences* 474 (2018) 20180050.
 - [64] K. Im, J.-H. Kang, Q.-H. Park, Universal impedance matching and the perfect transmission of white light, *Nature Photonics* 12 (2018) 143–149.
 - [65] S. Horsley, M. Artoni, G. C. La Rocca, Spatial kramers–kronig relations and the reflection of waves, *Nature Photonics* 9 (2015) 436–439.
 - [66] D. Ye, C. Cao, T. Zhou, J. Huangfu, G. Zheng, L. Ran, Observation of reflectionless absorption due to spatial kramers–kronig profile, *Nature communications* 8 (2017) 51.
 - [67] W. R. Sweeney, C. W. Hsu, A. D. Stone, Theory of reflectionless scattering modes, *Physical Review A* 102 (2020) 063511.
 - [68] J. Sol, A. Alhulaymi, A. D. Stone, P. Del Hougne, Reflectionless programmable signal routers, *Science Advances* 9 (2023) eadf0323.
 - [69] C. Guo, S. Fan, Reciprocity constraints on reflection, *Physical Review Letters* 128 (2022) 256101.
 - [70] A. D. Stone, W. R. Sweeney, C. W. Hsu, K. Wisal, Z. Wang, Reflectionless excitation of arbitrary photonic structures: A general theory, *Nanophotonics* 10 (2020) 343–360.
 - [71] C. Ferise, P. Del Hougne, S. Félix, V. Pagneux, M. Davy, Exceptional points of p t-symmetric reflectionless states in complex scattering systems, *Physical Review Letters* 128 (2022) 203904.
 - [72] H. Chen, C. T. Chan, P. Sheng, Transformation optics and metamaterials, *Nature materials* 9 (2010) 387–396.